

Gigahertz-rate-switchable wavefront shaping through integration of metasurfaces with photonic integrated circuit

Haozong Zhong^{1,†}, Yong Zheng^{1,†}, Jiacheng Sun^{1,†}, Zhizhang Wang^{1,†}, Rongbo Wu¹, Ling-en Zhang¹, Youting Liang¹, Qinyi Hua¹, Minghao Ning¹, Jitao Ji¹, Bin Fang^{1,†}, Lin Li^{1,†}, Tao Li^{1,†}, Ya Cheng^{1,†} and Shining Zhu^{1,†}

¹East China Normal University, School of Physics and Electronic Science, State Key Laboratory of Precision Spectroscopy, Shanghai, China

²Nanjing University, College of Engineering and Applied Sciences, National Laboratory of Solid State Microstructures, Nanjing, China

³China Jiliang University, College of Optical and Electronic Technology, Hangzhou, China

⁴Shanxi University, Collaborative Innovation Center of Extreme Optics, Taiyuan, China

⁵Chinese Academy of Sciences (CAS), Shanghai Institute of Optics and Fine Mechanics (SIOM), State Key Laboratory of High Field Laser Physics and CAS Center for Excellence in Ultra-Intense Laser Science, Shanghai, China

Abstract. Achieving spatiotemporal control of light at high speeds presents immense possibilities for various applications in communication, computation, metrology, and sensing. The integration of subwavelength metasurfaces and optical waveguides offers a promising approach to manipulate light across multiple degrees of freedom at high speed in compact photonic integrated circuit (PIC) devices. Here, we demonstrate a gigahertz-rate-switchable wavefront shaping by integrating metasurface, lithium niobate on insulator photonic waveguides, and electrodes within a PIC device. As proofs of concept, we showcase the generation of a focus beam with reconfigurable arbitrary polarizations, switchable focusing with lateral focal positions and focal length, orbital angular momentum light beams as well as Bessel beams. Our measurements indicate modulation speeds of up to the gigahertz rate. This integrated platform offers a versatile and efficient means of controlling the light field at high speed within a compact system, paving the way for potential applications in optical communication, computation, sensing, and imaging.

Keywords: metasurface; photonic integrated circuit; lithium niobate on insulator; high-speed modulation.

Received Jun. 29, 2023; revised manuscript received Sep. 25, 2023; accepted for publication Jan. 9, 2024; published online Feb. 2, 2024.

© The Authors. Published by SPIE and CLP under a Creative Commons Attribution 4.0 International License. Distribution or reproduction of this work in whole or in part requires full attribution of the original publication, including its DOI.

[DOI: [10.1117/1.AP.6.1.016005](https://doi.org/10.1117/1.AP.6.1.016005)]

1 Introduction

The remarkable multiple degrees of freedom (DOFs) possessed by light, including large bandwidth and high-speed transmission capabilities, make photonic technology an extremely promising platform for high-speed communication and high-performance computing in information science.^{1–3} Over the last decade, metasurfaces have emerged as an unprecedented approach for manipulating light in various DOFs using compact, artificial two-

dimensional nanostructures.^{4,5} Metasurfaces have demonstrated significant promise for a wide range of applications in both fundamental science and industry, including wavefront shaping,^{6,7} polarization control,^{8–10} imaging,^{11,12} spectrometry,^{13,14} and computation.¹⁵ Recently, considerable research efforts have been devoted to developing metasurfaces to achieve tunable or reconfigurable functionalities.^{3,16} A high-speed spatiotemporally controlled metasurface possesses the potential to facilitate novel physics and practical applications within the realm of photonic technology. Numerous materials and strategies have been proposed to empower tunable metasurfaces, including the utilization of phase-change materials, liquid crystal, thermo-optic effect, and electro-optic effect.^{17–22} However, effectively exploring

*Address all correspondence to Lin Li, lli@lps.ecnu.edu.cn; Tao Li, taoli@nju.edu.cn; Ya Cheng, ya.cheng@siom.ac.cn; Shining Zhu, zhusn@nju.edu.cn

[†]These authors contributed equally to this work.

tunability in multiple DOFs with high speed and sufficient efficiency remains a significant challenge in metasurface research.

On the other hand, photonic integrated circuits (PICs) represent an alternative to traditional electronic technologies by utilizing light. Diverse applications have been demonstrated with PICs, including high-speed optical communication, signal processing, computing, and emerging technologies in quantum, biomedicine, and sensing.^{23–28} Particularly, the advent of lithium niobate on insulator (LNOI) has propelled PICs as a promising platform for future high-speed electro-optic (EO) integrated devices,²⁹ such as high-performance modulators,^{30,31} frequency combs,^{32,33} polarization controllers,^{34,35} and quantum optics circuits.^{36,37} However, the full utilization of the DOFs of light in traditional two-dimensional PICs has not been realized, thereby limiting their application in optical information technologies. Recently, the integration of metasurfaces with waveguides has enabled PICs to manage multiple DOFs of light in both free space and waveguides with on-chip devices, providing a highly integrated platform for efficient photonics management.³⁸ A variety of applications have been reported with the guided-wave-driven metasurfaces, such as mode conversion,^{39,40} on-chip lenses,^{41,42} holography,^{43,44} OAM generators,^{3,45–48} as well as polarization control.^{49,50} Nevertheless, achieving high-speed wavefront shaping and switching capabilities through the integration of metasurfaces, photonic waveguides, and electrical circuits remains a significant scientific and technological challenge for PICs and metasurfaces.

In this work, we propose and demonstrate a gigahertz-rate-switchable wavefront shaping by integrating metasurfaces with LNOI PICs. An arbitrarily polarized light could be generated by combining a waveguide with two orthogonally propagated modes and nanoscatterers at the specific positions.⁴⁵ Through

the introduction of a Mach–Zehnder interferometer (MZI) and a phase shifter together with two pairs of electrodes, both the amplitude and the phase of the two orthogonal modes could be managed, enabling the generation of light with arbitrary polarizations spanning the entire surface of Poincaré sphere at high speed. Meanwhile, a well-designed polarization-dependent metasurface is introduced to achieve the desired functionality and facilitate high-speed modulation or switching. With this stratagem, switchable focusing with lateral focal positions and focal length, OAMs as well as Bessel beams are demonstrated. By effectively combining the propagation phase and geometric phase of birefringent nanostructures within this waveguide scheme, we demonstrate the switchability of these functionalities in arbitrary orthogonal polarizations. The switching speed reaches gigahertz rates, while the modulation speeds can be optimized to reach hundreds of gigahertz using tailored electrodes and LNOI PIC waveguides. This approach provides a versatile and efficient means of controlling light propagation in a compact and integrated system with simple electrical wiring and low power consumption, and promises important advantages in scenarios such as optical communication, computation, sensing, and imaging.

2 Results and Discussions

Figure 1(a) schematically shows the PIC-driven metasurface device. Two fundamental transverse-electric (TE_0) modes from LN ridge waveguides are transformed into two orthogonally propagated TE_0 modes in the slab waveguide. This transformation is achieved through the use of adiabatic tapers, as illustrated within the dashed square in Fig. 1(a). The zoomed-in view of the region is provided in Fig. 1(b). The electromagnetic wave in the slab waveguide can be expressed as

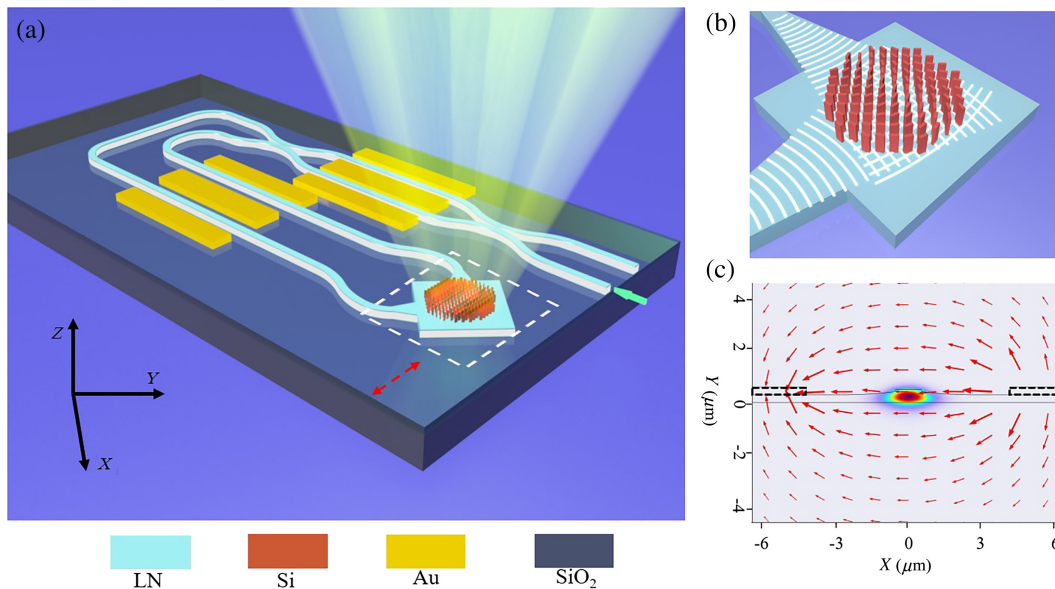


Fig. 1 (a) Schematic diagram of PIC-driven metasurface device with LNOI; the red arrow is the direction of optical axis. (b) The zoomed-in scheme of the integrated metasurface is depicted with the fictitious wavefront of the waveguide modes. (c) The simulated static electric field when 1 V is applied between the electrodes, superimposed with the simulated optical field profile of the TE_0 mode in the LN ridge waveguide. The black dashed lines indicate the electrodes. They have a height of 300 nm and are spaced apart by $6.5 \mu\text{m}$. The top width of the LN ridge waveguide is $1 \mu\text{m}$, and the etch depth is 210 nm.

$$E_{xy} = \begin{bmatrix} Ae^{i(\varphi_x + x_n\beta_x)} \\ Be^{i(\varphi_y + y_n\beta_y)} \end{bmatrix}, \quad (1)$$

where A , B , φ_x , and φ_y represent the amplitudes and initial phases of the two guided waves, respectively. β_x and β_y are the propagation constants of the guided waves in slab waveguide. The near orthogonal nature of the two transverse components of the electric field enables the synthesis of a wide range of polarization states across the entire surface of the Poincaré sphere. This synthesis is achieved by manipulating the amplitudes and phase lags ($\Delta\varphi = \varphi_x + x_n\beta_x - \varphi_y - y_n\beta_y$) of the two components. To enable high-speed modulation, an electrically controlled MZI and a phase shifter are utilized to modulate the amplitude and phase of the two components. Subsequently, guided-wave-driven silicon metasurfaces are strategically positioned on the slab waveguide, with specific uniform polarizations, to generate a variety of electrically controlled functionalities. These functionalities can be manipulated at high speeds, offering enhanced control and versatility.

The device is designed and fabricated on an x -cut LNOI platform to provide the best electro-optical performance. Considering the anisotropy of x -cut LN, both TE_0 modes are specifically designed to propagate at a 45 deg angle to the short optical axis of LN. This arrangement ensures that the wave vectors $\beta_x = \beta_y$ and maintains a symmetric polarization distribution, as shown in Fig. 1(a). To precisely get the polarization distribution on the waveguide, we perform a finite-difference time-domain (FDTD) simulation to get the amplitude and phase evolution over the slab waveguide at the experiment wavelength of 1550 nm, as shown in Fig. S1 in the [Supplementary Material](#). Directional couplers (DCs) are employed to achieve the tunable splitting function of the MZI, having a center-to-center spacing of 4.5 μm and a length of 300 μm . Meanwhile, ground–signal–ground (G–S–G) electrodes are used in the inner and outer phase shifters of the MZI to induce phase shifts in a single-drive push–pull configuration, so that the electric field induces phase shifts in both arms with equal magnitude but opposite signs. The simulated optical field profile of the TE_0 mode in the LN ridge waveguide together with the static electric field between the electrodes is shown in Fig. 1(c), exhibiting a good overlap of the two fields.

The PIC-driven metasurface is initially investigated to showcase a functionality with arbitrary reconfigurable polarization. In order to demonstrate the feasibility of this approach, a focusing beam achieved with a silicon nanocylinder metasurface is investigated. The Jones matrix of isotropic silicon nanocylinders is given by $e^{i\alpha} \begin{bmatrix} 1 & 0 \\ 0 & 1 \end{bmatrix}$, where α is the propagation phase of the nanocylinders. The electromagnetic wave extracted to free space by silicon cylinders can be expressed as

$$\begin{bmatrix} E_{x\text{out}} \\ E_{y\text{out}} \end{bmatrix} = e^{i\alpha} \begin{bmatrix} 1 & 0 \\ 0 & 1 \end{bmatrix} \begin{bmatrix} Ae^{i(\varphi_x + x_n\beta_x)} \\ Be^{i(\varphi_y + y_n\beta_y)} \end{bmatrix} = e^{i\alpha} \begin{bmatrix} Ae^{i(\varphi_x + x_n\beta_x)} \\ Be^{i(\varphi_y + y_n\beta_y)} \end{bmatrix}. \quad (2)$$

Thus, the phase profile of the free-space electromagnetic wave depends on the location of the silicon cylinders. On the other hand, to generate a focused beam in free space, the phase of light scattered from the metasurface has a distribution described as

$$\varphi(x, y) = -\frac{2\pi}{\lambda} \left(\sqrt{x^2 + y^2 + f^2} - f \right), \quad (3)$$

where f is the distance between the device plane and the focal plane, i.e., the focal length. Then, the metasurface is constructed by arranging this set of silicon cylinders on top of the slab waveguide to extract the desired polaritons state with the phase profile for focusing. Here, the focal length is designed to be $f = 50 \mu\text{m}$. The silicon cylinders have identical dimensions, with a radius of $R = 100 \text{ nm}$ and a height of $H = 1000 \text{ nm}$. The detailed design process of the metasurface array and the fabrication process are described in sections 2 and 7 in the [Supplementary Material](#), respectively. Figure 2(a) displays the microscope image of the fabricated device, where the electrodes have a length of 5 mm and a gap of 6.5 μm between them. Figure 2(b) shows the scanning electron microscopy (SEM) image of the fabricated metasurface. We captured the three-dimensional (3D) scattered light-field distribution above the device using a home-built optical setup (section 6 in the [Supplementary Material](#)). An image recorded at the $x - z$ plane is illustrated in Fig. 2(c), revealing a distinct focal spot with a full width at half-maximum (FWHM) of $\sim 2 \mu\text{m}$.

By adjusting the voltages applied to the electrodes of the MZI and the phase shifter, the polarization state of the focal spot can be dynamically manipulated. To evaluate the performance of the reconfiguration polarizations of our device, two triangle wave signals with frequencies of 1 and 100 kHz are applied to the electrodes of the MZI and phase shifter, respectively. The peak-to-peak drive voltages (V_{pp}) are set to 9.2 V, corresponding to a phase shift of $\sim 2\pi$. The blue dots in Fig. 2(d) depict the measured sampling points on the Poincaré sphere (the schematic diagram of the experimental setup is presented in section 6 in the [Supplementary Material](#) and the corresponding measured Stokes parameters are presented in section 7 in the [Supplementary Material](#)), representing the polarization states of the focal spot. The polarization extinction ratio (PER) was measured to be $\sim 20 \text{ dB}$ (section 3 in the [Supplementary Material](#)). The majority of the Poincaré sphere's surface is covered, with the exception of two areas near the north and south poles. This deviation is mainly due to imperfections in the fabrication process, resulting in a splitting ratio of the DC in the MZI that deviates from the ideal 50:50 ratio. This issue can be addressed by employing an additional electrically controlled interferometer to improve the splitting ratio.³⁴ Figure 2(e) depicts the good stability of the generated polarization state, indicating its robustness. Figure 2(f) showcases the switching performance between two polarizations, highlighting the high repeatability of polarization generation. By adjusting the voltages applied to the electrodes, transitions between any polarized states within the blue region of Fig. 2(d) can be achieved with the same level of stability and repeatability. These results exhibit the promising capability of our device for wavefront shaping with good control over reconfigurable arbitrary polarization states.

In addition to enabling the generation of a single wavefront with reconfigurable polarizations, this scheme has the capability to achieve high-speed switchable multifunctionalities through the incorporation of polarization-dependent metasurfaces, which holds tremendous potential for a wide range of applications. To exhibit this capability, we first introduce a geometric metasurface to the PIC device, enabling the realization of two focal points with orthogonal polarizations at different lateral

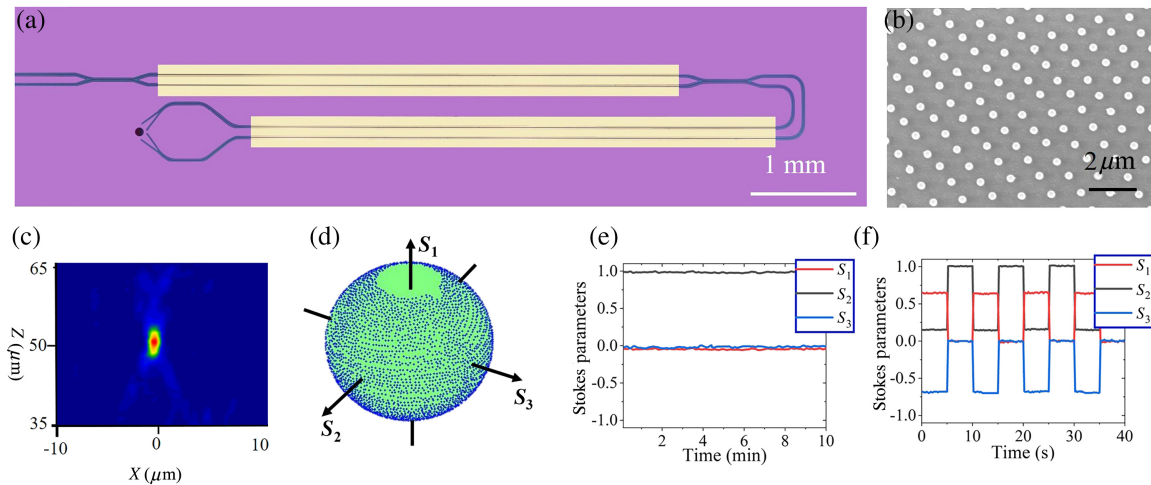


Fig. 2 (a) The microscope image of the fabricated device. The length of the two sets of electrodes is 0.5 mm. (b) SEM image of the fabricated metasurface on the waveguide. (c) The measured intensity profile at the $x - z$ plane. (d) The measured polarization states on the Poincaré sphere of the focal spot. The blue dots on the Poincaré sphere represent the polarization states of the focal spot obtained from experimental testing. (e) Stokes parameters of one of the generated polarization state (45 deg linear polarization as shown in the inset) as a function of time. (f) Stokes parameters by switching between two generated polarization states.

positions. The metasurface is composed of two sets of silicon nanobars as shown in Fig. 3(a), which are designed to realize two foci based on left circular polarization (LCP) and right circular polarization (RCP) states, respectively. The two sets of nanostructures are spatially multiplexed with a near face centered square unit with the period of the effective wavelength of the TE_0 mode in the slab waveguide (section 2 in the [Supplementary Material](#)). In this arrangement, the two sets of nanostructures are positioned in locations with the same local polarization ψ . By adjusting the voltages applied to the electrodes, the local polarization ψ can be dynamically switched between LCP and RCP states. Through this control mechanism, the scattered light can be switched between the two designed focal spots, respectively. Meanwhile, the unwanted co-polarization noise will be greatly suppressed due to the phase mismatch.⁴⁵

In the experiment, the silicon nanobars have a uniform length (L) of 300 nm, width (W) of 100 nm, and height (H) of 1000 nm. The corresponding SEM image of fabricated metasurface on the slab waveguide is shown in Fig. 3(b). The two foci are designed at $x = 5 \mu\text{m}$ and $x = -5 \mu\text{m}$, with the center of the metasurface array serving as the origin of coordinates. The focal length is set to $f = 50 \mu\text{m}$ for both spots. Figures 3(f)–3(h) show the recorded images of the foci at different voltages for the phase control. The voltage of the MZI is offset to ensure equal amplitudes in the two arms. By adjusting the voltages applied to the phase shifter, the scattered energy gradually transitions between the two focal spots. The experimental results align well with the calculated images based on the corresponding designed local polarizations, as shown in Figs. 3(c)–3(e). This result demonstrates the effectiveness of the adopted strategy. A video illustrating the dynamic modulation process is provided in the [Supplementary Material](#).

To accurately assess the modulation performance, we integrated the recorded focal intensities in Fig. 3 and observed

an extinction ratio of ~ 10.2 dB. The electro-optical tunability of the device was evaluated by directing the light from one focus to a high-speed photon detector [FINISAR XPDV21x0(RA)] for analysis (section 6 in the [Supplementary Material](#)). The measured V_π of the device is ~ 4.6 V as shown in Fig. 3(i) (corresponding to a $V_\pi \cdot L$ of 2.3 V·cm). Figure 3(j) presents the peak electro-optic modulation amplitude for frequencies up to 2 GHz. The result indicates the electro-optic bandwidth of the sample is around 1.4 GHz, providing clear evidence of its gigahertz tunability. Furthermore, the switching speed could be further improved to hundreds of gigahertz by carefully optimized the electrodes and waveguide design.

Apart from the ability to vary the lateral positions of the focal points, this scheme also enables dynamic switching of the focal length, which holds great significance and has garnered plenty of attention.^{51,52} To demonstrate this concept, two different sets of nanostructures are designed, resulting in two focal points with focal lengths of $f = 35 \mu\text{m}$ and $f = 50 \mu\text{m}$, respectively. Figures 4(d)–4(f) show the recorded images of the foci by varying the voltage applied to the phase shifter, which agrees well with the calculated results [Figs. 4(a)–4(c)]. The focal points can be dynamically adjusted between these two states or any intermediate states. These integrated lenses with high-speed switchable focal positions and lengths hold promise for future high-speed portable imaging applications, opening up new possibilities in the field.

The high-speed switchable wavefront-shaping technique holds immense potential for various applications such as optical communications, imaging, optical computation, sensing, and more. Particularly, the generation of optical orbital angular momentum (OAM) with a large modulation bandwidth is of significant importance in the realm of optical communication.⁵³ We replace the focus beams with two OAMs with different topological numbers and locations by mapping the required phase distributions to the two sets of metasurfaces. Figures 4(j)–4(l)

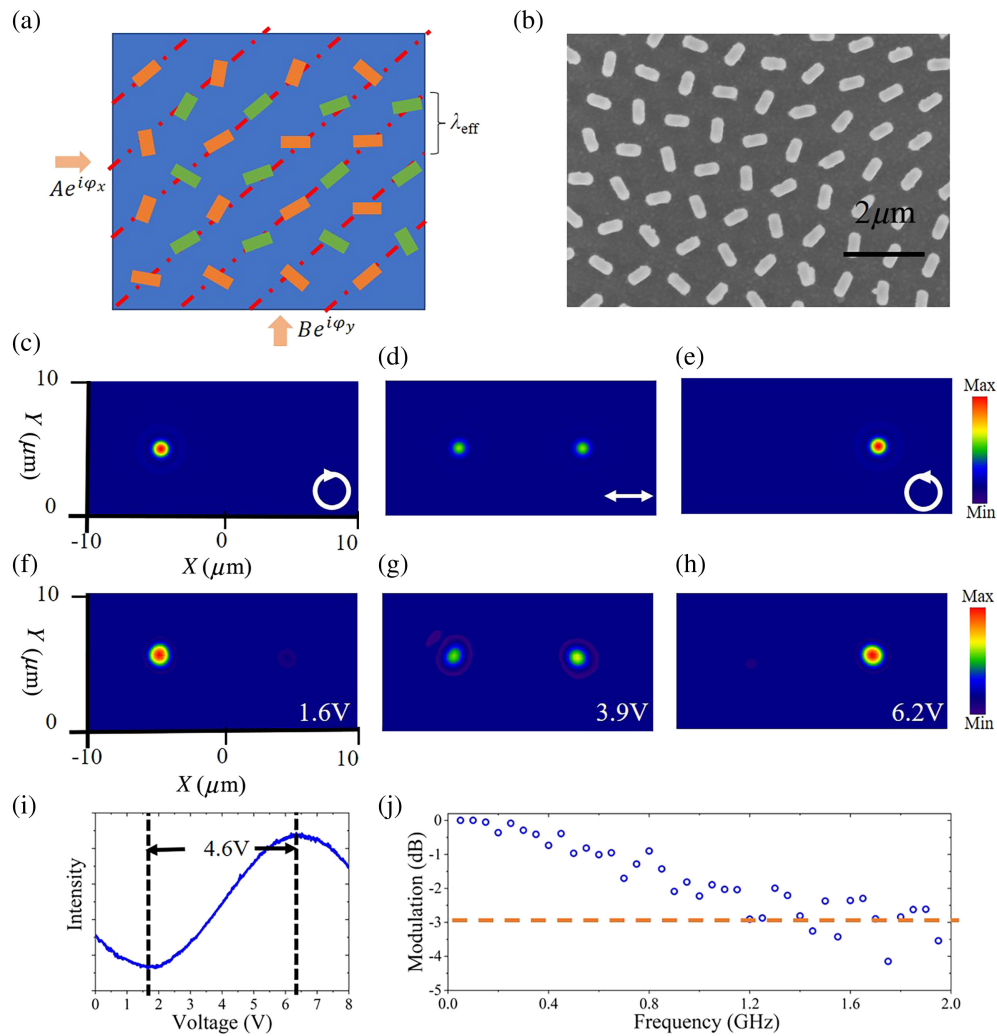


Fig. 3 (a) The schematic of the switchable metasurface design. (b) SEM image of the fabricated metasurface structure. (c)–(e) Calculated results of foci under different local polarization states ψ depicted in the figures. (f)–(h) The corresponding experimental results. The polarization states are realized by applying different voltages shown in the figures to the electrodes, respectively. (i) The intensity of the right focus in (f) as a function of applied voltage. (j) Peak electro-optic amplitude for modulation frequencies up to 2 GHz (Video 1, MP4, 120 KB [URL: <https://doi.org/10.1117/1.AP.6.1.016005.s1>]).

show the typical recorded OAM images by varying the voltages applied to the electrode of the phase shifter, which agree well with the calculated results under certain corresponding polarizations, shown in Figs. 4(g)–4(i). The left OAM beam is designed with $l = +1$ in LCP state and the right one is designed with $l = -1$ in RCP state. The results exhibit that the integrated device has the capability to dynamically manipulate OAM beams with various topological numbers, offering promising applications in optical communications and manipulations. These findings indicate the feasibility of utilizing a geometric phase-based spatial multiplexing multichannel device within our platform.

The aforementioned multifunction switchable devices are designed with a geometric phase constraint limited to circular polarizations. Indeed, it is important to note that this constraint can be extended to encompass any arbitrary orthogonal polarization states by considering the geometric phase and propagation

phase of birefringent nanostructures for free-space light.⁵⁴ It holds significant importance in applications involving polarization optics, offering enhanced versatility and adaptability. However, this scheme is still awaiting clarification in the guided-wave-driven metasurfaces due to the overlapping of the in-plane waveguide mode and the nanostructures. Meanwhile, the scattering efficiency of the nanostructures on the waveguide exhibits a strong dependence on their size, and this behavior differs significantly from the transmission characteristics of metasurfaces in the free-space configuration. Here, we present the successful engineering and dynamic switching of a wavefront in arbitrary polarization states with the metasurface on a PIC device. When a birefringent nanostructure scatters the waveguide mode with an arbitrary local polarization of Ψ_1 , the scattered light can be decomposed into a pair of orthogonal polarization states, Ψ_2^+ and Ψ_2^- , respectively. The two decomposed components can be expressed as

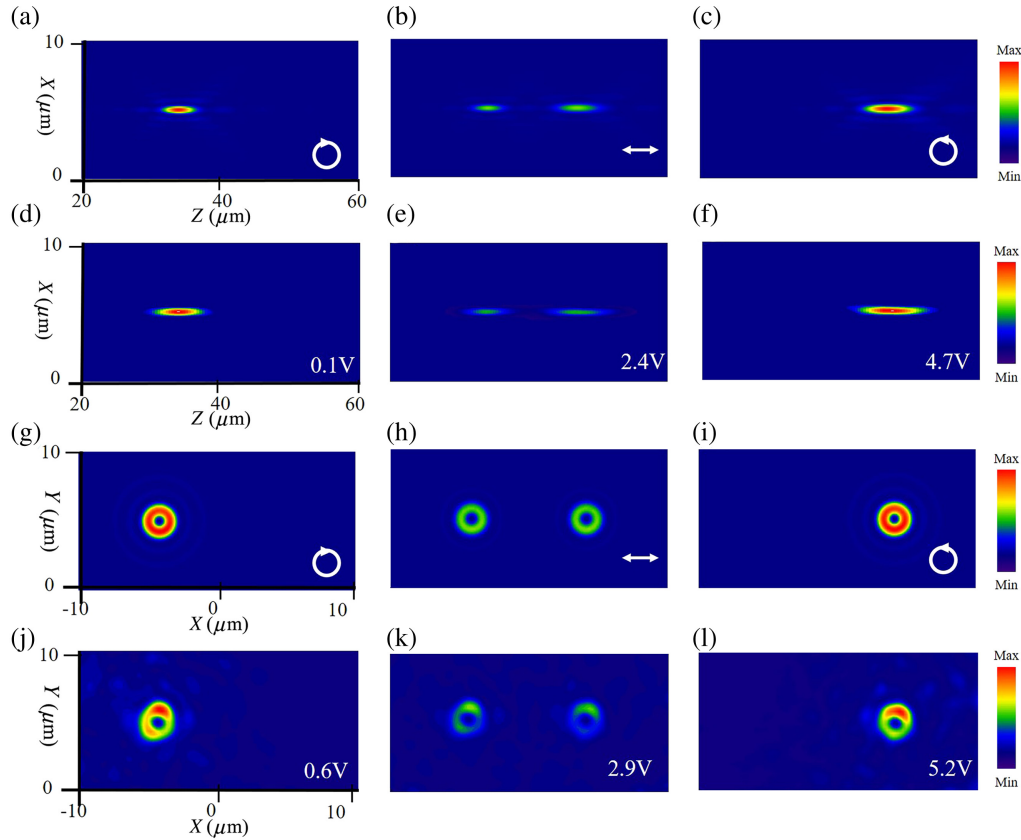


Fig. 4 (a)–(c) Calculated results of switchable focal length under different local polarization states depicted in the figures. (d)–(f) The corresponding experimental results were realized by applying different voltages to the electrodes as shown in the figures, respectively. (g)–(i) Calculated results of switchable OAM beams with switchable topological charges under different local polarization states depicted in the figures. (j)–(l) The corresponding experimental results were realized by applying different voltages to the electrodes as shown in the figures, respectively.

$$O^\pm e^{i\phi^\pm} = \hat{\xi}_2^\pm \begin{bmatrix} T_x & T_{xy} \\ T_{xy} & T_y \end{bmatrix} \Psi_1, \quad (4)$$

where $\hat{\xi}_2^\pm$ represents the projection operators for the polarization states of Ψ_2^+ and Ψ_2^- , respectively. O^\pm and ϕ^\pm are the amplitude and phase of the scattered light after the projection operation, respectively. Considering the physical characteristics of linear birefringent metasurfaces and their ability to consistently convert input polarization states into output polarization states with arbitrary phase delays, it is necessary for the input and output polarization states to be a pair of orthogonal polarization states.

On the other hand, the required Jones matrix $\begin{bmatrix} T_x & T_{xy} \\ T_{xy} & T_y \end{bmatrix}$ could be implemented by utilizing rectangular nanostructures and adjusting their dimensions to impose arbitrary phase delays upon two orthogonal polarization states. The aforementioned outcome can be comprehended as the amalgamation of both the propagation and geometric phases within a singular component. By simultaneously adjusting the size and orientation of the birefringent nanostructure, it becomes possible to impart desired phases onto the orthogonal polarization states. To design the nanostructure with the desired Jones matrix, we built a phase-amplitude response library with regard to the rectangular nanostructure dimensions on slab waveguide using full-wave

simulations (section 5 in the [Supplementary Material](#)). Here, the width and the length of the nanostructure are varied between 100 and 500 nm and the height is 1000 nm. The amplitude and the phase of the scattering upon different dimensions are shown in Figs. 5(a) and 5(b). A genetic algorithm is employed to retrieve the required dimensions for the desired Jones matrix with near-uniform scattering intensity. Finally, arbitrary phase profiles in the independent polarization channels could be realized by spatially arranging the retrieved nanostructures.

Similar to the geometric phase-based metasurfaces demonstrated above, by varying the polarization distribution within the planar waveguide region, we can switch the wavefronts designed upon the arbitrary independent polarization channels. As an example, here we demonstrate an integrated generation of switchable Bessel beams with arbitrary polarizations, which have garnered significant interest across a wide range of research fields. The polarization states of the two Bessel beams are designed with $1/\sqrt{5}[2 e^{i\pi/4}]^T$ and $1/\sqrt{5}[1 2e^{5i\pi/4}]^T$, respectively. Figure 5(c) depicts the SEM images of fabricated sample. Figures 5(g)–5(i) illustrate the featured images through the adjustment of voltages applied to the MZI and the phase shifter. The formation of Bessel beams in different directions (± 5 deg) of the scattered light is clearly shown, and these adjustments align with the calculation results displayed in Figs. 5(d)–5(f), considering the corresponding polarizations.

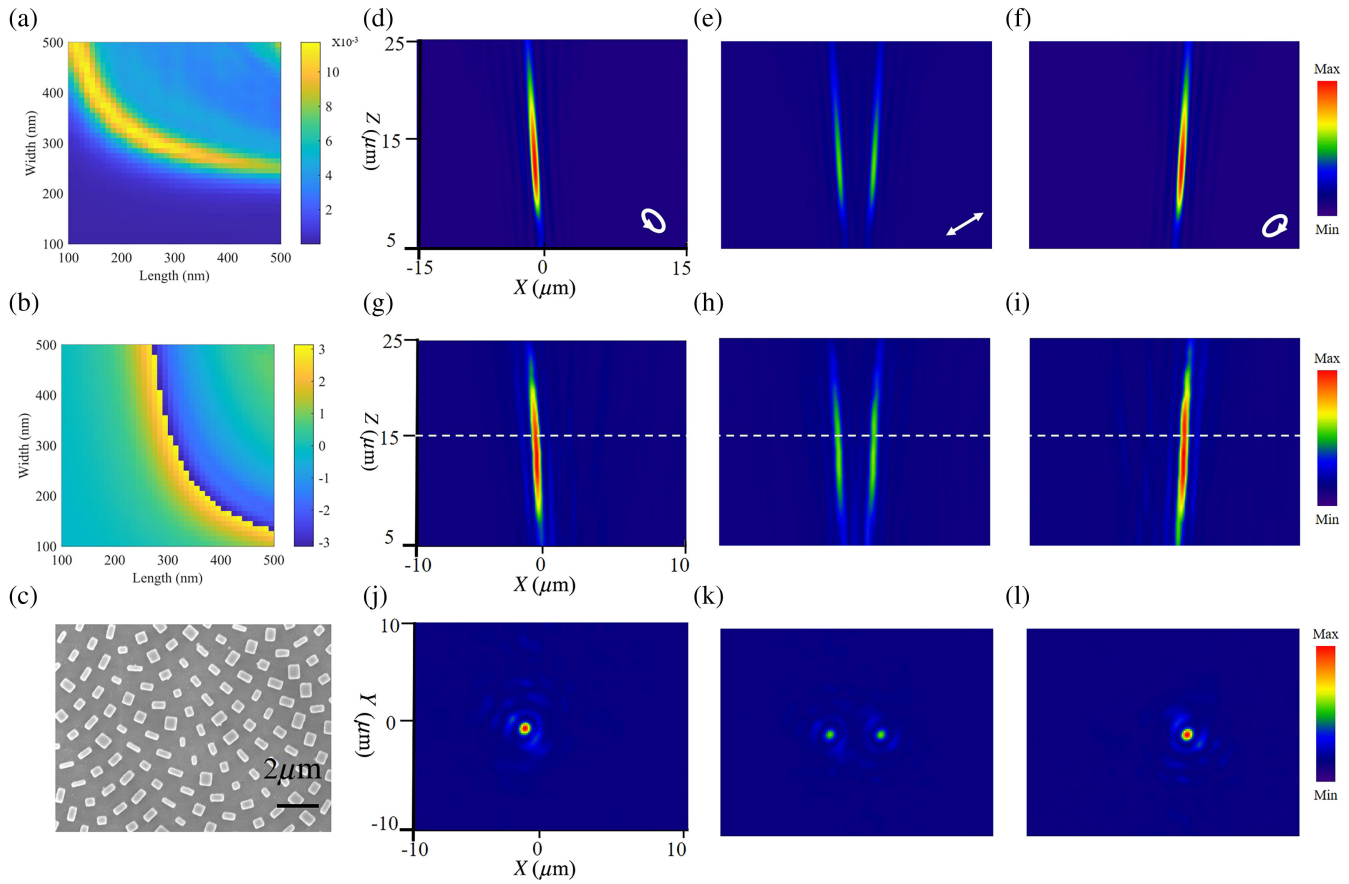


Fig. 5 (a) The simulated intensity and (b) phase of the scattered light when the rectangular nanostructure's length and width vary from 100 to 500 nm. (c) SEM image of the fabricated metasurface for Bessel beams. (d)–(f) Calculated results of switchable Bessel beams under different local polarization states depicted in the figures. (g)–(i) The corresponding experimental results by adjusting voltages applied to the electrodes, respectively. (j)–(l) The corresponding cross-sectional images along the white dashed lines in (g)–(i), respectively.

Figures 5(j)–5(l) show the recorded lateral images along the white dashed lines in Figs. 5(g)–5(i), respectively. The integrated generation of switchable nondiffracting Bessel beams with arbitrary polarization states demonstrates the feasibility of our method for achieving switchable functionalities in any arbitrary polarization state. Moreover, it introduces exciting new prospects for applications involving special beam characteristics.

We have demonstrated the capability of wavefront shaping and switching upon any orthogonal polarization states. Indeed, this high-speed switchable scheme could also be extended to nonorthogonal polarization states as well. By incorporating complex unit cell, interleave design, as well as artificial intelligence, the traditional limitation of two independent orthogonal channels could be broken, enabling the realization of more polarization-determined and switchable channels.⁹ This strategy not only enables the generation of specialized optical beams but also facilitates the implementation of various switchable and complex functionalities. In addition to generate switchable wavefronts in uniform polarization states, the PIC-driven metasurface exhibits the potential to produce complex vector wavefronts. Furthermore, this approach can also utilize alternative high-speed modulation PIC platforms and mechanisms, in

addition to LNOI, such as carrier depletion, enabling increased levels of integration and compatibility with CMOS technology. The out-of-plane extraction efficiency of the integrated metasurface in our device can reach 11% with numerical simulation, which can be further improved by optimizing the geometric parameters of the metasurfaces and the waveguide^{50,55} (section 8 in the [Supplementary Material](#)). These factors expand the applicability across a wide range of fields and applications.

3 Conclusion

We have proposed and demonstrated an integrated electro-optical platform with PIC-driven metasurface on LNOI. By integrating an electrically controlled MZI and a phase shifter, we constructed a focusing beam with high-speed adjustable polarizations across almost the entire surface of the Poincaré sphere. Based on the reconfigurable polarizations across the waveguide, switchable focusing beams with lateral focal positions and focal lengths, OAM beams and Bessel beams were demonstrated. Our approach opens up possibilities for achieving more switchable functionalities with complex polarizations. The modulation bandwidth is measured to be 1.4 GHz and it has the potential to be improved to hundreds of gigahertz based on

the electro-optical effect of LN. The demonstrated high-speed switchable PIC-driven metasurface provides a promising platform for a variety of applications in high-capacity optical communication, fast optical computation, imaging, and sensing. This integrated platform offers significant opportunities for advancing these fields and enabling a wide range of practical applications.

Disclosures

The authors declare no conflicts of interest.

Code and Data Availability

Structural parameters and simulated and experimental data have been provided within the main text and [Supplementary Material](#) of this paper. All the other data that support the findings of this study are available from the corresponding authors upon reasonable request.

Acknowledgments

This work was supported by the National Key R&D Program of China (Grant No. 2019YFA0705000), the National Natural Science Foundation of China (Grant Nos. 12192251, 12274134, 12174186, and 62288101), the Science and Technology Commission of Shanghai Municipality (Grant No. 21DZ1101500), the Shanghai Municipal Education Commission (Grant No. 2023ZKZD35), and the Shanghai Pujiang Program (Grant No. 20PJ1403400).

References

1. A. M. Shaltout, V. M. Shalae, and M. L. Brongersma, "Spatiotemporal light control with active metasurfaces," *Science* **364**, eaat3100 (2019).
2. T. Zhou et al., "Large-scale neuromorphic optoelectronic computing with a reconfigurable diffractive processing unit," *Nat. Photonics* **15**, 367–373 (2021).
3. W. Shi, Y. Tian, and A. Gervais, "Scaling capacity of fiber-optic transmission systems via silicon photonics," *Nanophotonics* **9**, 4629–4663 (2020).
4. N. Yu and F. Capasso, "Flat optics with designer metasurfaces," *Nat. Mater.* **13**, 139–150 (2014).
5. A. H. Dorrah and F. Capasso, "Tunable structured light with flat optics," *Science* **376**, eabi6860 (2022).
6. N. Yu et al., "Light propagation with phase discontinuities: generalized laws of reflection and refraction," *Science* **334**, 333–337 (2011).
7. L. Deng et al., "Structured light generation using angle-multiplexed metasurfaces," *Adv. Opt. Mater.* **11**(16), 2300299 (2023).
8. M. Liu et al., "Multifunctional metasurfaces enabled by simultaneous and independent control of phase and amplitude for orthogonal polarization states," *Light Sci. Appl.* **10**, 107 (2021).
9. A. Xiong et al., "Breaking the limitation of polarization multiplexing in optical metasurfaces with engineered noise," *Science* **379**, 294–299 (2023).
10. L. Deng et al., "On-demand mode conversion and wavefront shaping via on-chip metasurfaces," *Adv. Opt. Mater.* **10**, 2200910 (2022).
11. S. Colburn, A. Zhan, and A. Majumdar, "Metasurface optics for full-color computational imaging," *Sci. Adv.* **4**, eaar2114 (2018).
12. T. Li et al., "Revolutionary meta-imaging: from superlens to metalens," *Photonics Insights* **2**, R01 (2023).
13. M. Faraji-Dana et al., "Compact folded metasurface spectrometer," *Nat. Commun.* **9**, 4196 (2018).
14. F. Yesilkoy et al., "Ultrasensitive hyperspectral imaging and bio-detection enabled by dielectric metasurfaces," *Nat. Photonics* **13**, 390–396 (2019).
15. A. Cordaro et al., "Solving integral equations in free space with inverse-designed ultrathin optical metagratings," *Nat. Nanotechnol.* **18**, 365–372 (2023).
16. Q. He, S. Sun, and L. Zhou, "Tunable/reconfigurable metasurfaces: physics and applications," *Research* **2019**, 16 (2019).
17. G. K. Shirmanesh et al., "Dual-gated active metasurface at 1550 nm with wide (> 300) phase tunability," *Nano Lett.* **18**, 2957–2963 (2018).
18. J. Park et al., "All-solid-state spatial light modulator with independent phase and amplitude control for three-dimensional LiDAR applications," *Nat. Nanotechnol.* **16**, 69–76 (2021).
19. A. Komar et al., "Dynamic beam switching by liquid crystal tunable dielectric metasurfaces," *ACS Photonics* **5**, 1742–1748 (2018).
20. M. Rahmani et al., "Reversible thermal tuning of all-dielectric metasurfaces," *Adv. Funct. Mater.* **27**, 1700580 (2017).
21. I.-C. Benea-Chelmus et al., "Gigahertz free-space electro-optic modulators based on Mie resonances," *Nat. Commun.* **13**, 3170 (2022).
22. H. Weigand et al., "Enhanced electro-optic modulation in resonant metasurfaces of lithium niobate," *ACS Photonics* **8**, 3004–3009 (2021).
23. E. A. Rank et al., "Toward optical coherence tomography on a chip: *in vivo* three-dimensional human retinal imaging using photonic integrated circuit-based arrayed waveguide gratings," *Light Sci. Appl.* **10**, 6 (2021).
24. J. C. Norman et al., "Perspective: the future of quantum dot photonic integrated circuits," *APL Photonics* **3**, 030901 (2018).
25. M. Xu et al., "High-performance coherent optical modulators based on thin-film lithium niobate platform," *Nat. Commun.* **11**, 3911 (2020).
26. A. Liu et al., "Wavelength division multiplexing based photonic integrated circuits on silicon-on-insulator platform," *IEEE J. Sel. Top. Quantum Electron.* **16**, 23–32 (2009).
27. J. Mower et al., "High-fidelity quantum state evolution in imperfect photonic integrated circuits," *Phys. Rev. A* **92**, 032322 (2015).
28. S. Arafin and L. A. Coldren, "Advanced InP photonic integrated circuits for communication and sensing," *IEEE J. Sel. Top. Quantum Electron.* **24**, 6100612 (2017).
29. Y. Qi and Y. Li, "Integrated lithium niobate photonics," *Nanophotonics* **9**, 1287–1320 (2020).
30. A. Wang et al., "Integrated lithium niobate electro-optic modulators operating at CMOS-compatible voltages," *Nature* **562**, 101–104 (2018).
31. M. He et al., "High-performance hybrid silicon and lithium niobate Mach-Zehnder modulators for 100 Gbit s⁻¹ and beyond," *Nat. Photonics* **13**, 359–364 (2019).
32. M. Zhang et al., "Broadband electro-optic frequency comb generation in a lithium niobate microring resonator," *Nature* **568**, 373–377 (2019).
33. A. Wang et al., "Monolithic lithium niobate photonic circuits for Kerr frequency comb generation and modulation," *Nat. Commun.* **10**, 978 (2019).
34. Z. Lin et al., "High-performance polarization management devices based on thin-film lithium niobate," *Light Sci. Appl.* **11**, 93 (2022).
35. X. Sun et al., "Thin-film lithium niobate polarization modulator without polarization diversity," *Opt. Express* **30**, 30592–30599 (2022).
36. U. A. Javid et al., "Ultrabroadband entangled photons on a nanophotonic chip," *Phys. Rev. Lett.* **127**, 183601 (2021).
37. A. W. Elshaari et al., "Hybrid integrated quantum photonic circuits," *Nat. Photonics* **14**, 285–298 (2020).
38. A. Boes et al., "Status and potential of lithium niobate on insulator (LNOI) for photonic integrated circuits," *Laser Photonics Rev.* **12**, 1700256 (2018).

39. Y. Meng et al., "Optical meta-waveguides for integrated photonics and beyond," *Light Sci. Appl.* **10**, 235 (2021).
40. Z. Li et al., "Controlling propagation and coupling of waveguide modes using phase-gradient metasurfaces," *Nat. Nanotechnol.* **12**, 675–683 (2017).
41. S. Kim et al., "Photonic waveguide to free-space Gaussian beam extreme mode converter," *Light Sci. Appl.* **7**, 72 (2018).
42. A. Xie et al., "Bifocal focusing and polarization demultiplexing by a guided wave-driven metasurface," *Opt. Express* **29**, 25709–25719 (2021).
43. Y. Shi et al., "Augmented reality enabled by on-chip meta-holography multiplexing," *Laser Photonics Rev.* **16**, 2100638 (2022).
44. Y. Ding et al., "Metasurface-dressed two-dimensional on-chip waveguide for free-space light field manipulation," *ACS Photonics* **9**, 398–404 (2022).
45. A. Fang et al., "Manipulating guided wave radiation with integrated geometric metasurface," *Nanophotonics* **11**, 1923–1930 (2021).
46. Z. Xie et al., "Ultra-broadband on-chip twisted light emitter for optical communications," *Light Sci. Appl.* **7**, 18001 (2018).
47. X. Guo et al., "Molding free-space light with guided wave-driven metasurfaces," *Sci. Adv.* **6**, eabb4142 (2020).
48. N. Zhou et al., "Ultra-compact broadband polarization diversity orbital angular momentum generator with $3.6 \times 3.6 \mu\text{m}^2$ footprint," *Sci. Adv.* **5**, eaau9593 (2019).
49. L. Li et al., "Plasmonic polarization generator in well-routed beaming," *Light Sci. Appl.* **4**, e330 (2015).
50. J. Ji et al., "Metasurface-enabled on-chip manipulation of higher-order poincaré sphere beams," *Nano Lett.* **23**, 2750–2757 (2023).
51. J. Kim et al., "Tunable metasurfaces towards versatile metalenses and metaholograms: a review," *Adv. Photonics* **4**, 024001 (2022).
52. M. Y. Shalaginov et al., "Reconfigurable all-dielectric metalens with diffraction-limited performance," *Nat. Commun.* **12**, 1225 (2021).
53. J. B. Mueller et al., "Metasurface polarization optics: independent phase control of arbitrary orthogonal states of polarization," *Phys. Rev. Lett.* **118**, 113901 (2017).
54. A. M. Yao and M. J. Padgett, "Orbital angular momentum: origins, behavior and applications," *Adv. Opt. Photonics* **3**, 161–204 (2011).
55. R. Wu et al., "High-production-rate fabrication of low-loss lithium niobate electro-optic modulators using photolithography assisted chemo-mechanical etching (PLACE)," *Micromachines* **13**, 378 (2022).
56. B. Schaefer et al., "Measuring the Stokes polarization parameters," *Am. J. Phys.* **75**(2), 163–168 (2007).
57. J. Lin et al., "Advances in on-chip photonic devices based on lithium niobate on insulator," *Photonics Res.* **8**(12), 1910–1936 (2020).

Haozong Zhong received his BS and MS degrees from Jiangxi Normal University, China, in 2018 and 2021, respectively. He is currently a PhD candidate in the State Key Laboratory of Precision Spectroscopy, East China Normal University. His research interest is nanophotonics, and he is mainly engaged in the related research of optical metasurfaces.

Yong Zheng received his bachelor's degree in optoelectronic information science and engineering from Jiangnan University, Wuxi, China, in 2020. He is currently a PhD candidate in the Department of Optics at East China Normal University, with a main research focus on photonic neural networks for large-scale lithium niobate photonic integrated chips.

Jiacheng Sun received his bachelor's degree in physics from Nanjing University, Jiangsu, China, in 2021. He is currently a PhD candidate at the College of Engineering and Applied Science, Nanjing University, Jiangsu, China. His research mainly focuses on the design and fabrication of metasurfaces.

Lin Li is a professor in the State Key Laboratory of Precision Spectroscopy, East China Normal University. He received his PhD from Nanjing University in 2014. His research interests include nanophotonics, integrated photonics, and quantum optics.

Tao Li is a professor in the College of Engineering and Applied Sciences at Nanjing University. He received his PhD from Nanjing University in 2005. His research interests include metamaterials, plasmonics, and nanophotonic integrations.

Biographies of the other authors are not available.